— RESEARCH ARTICLE —

Chemical Exchange Saturation Transfer MRI for Differentiating Radiation Necrosis From Tumor Progression in Brain Metastasis—Application in a Clinical Setting

Hatef Mehrabian, PhD,[1]* ⓘ Rachel W. Chan, PhD,[1] ⓘ Arjun Sahgal, MD,[2] Hanbo Chen, MD,[2] Aimee Theriault, BSc,[2] Wilfred W. Lam, PhD,[1] ⓘ Sten Myrehaug, MD,[2] Chia-Lin Tseng, MD,[2] Zain Husain, MD,[2] Jay Detsky, MD,[2] Hany Soliman, MD,[2] and Greg J. Stanisz, PhD[1,3,4]

Background: High radiation doses of stereotactic radiosurgery (SRS) for brain metastases (BM) can increase the likelihood of radiation necrosis (RN). Advanced MRI sequences can improve the differentiation between RN and tumor progression (TP).
Purpose: To use saturation transfer MRI methods including chemical exchange saturation transfer (CEST) and magnetization transfer (MT) to distinguish RN from TP.
Study Type: Prospective cohort study.
Subjects: Seventy patients (median age 60; 73% females) with BM (75 lesions) post-SRS.
Field Strength/Sequence: 3-T, CEST imaging using low/high-power (saturation $B_1 = 0.52$ and 2.0 μT), quantitative MT imaging using $B_1 = 1.5$, 3.0, and 5.0 μT, WAter Saturation Shift Referencing (WASSR), WAter Shift And B_1 (WASABI), T_1, and T_2 mapping. All used gradient echoes except T_2 mapping (gradient and spin echo).
Assessment: Voxel-wise metrics included: magnetization transfer ratio (MTR); apparent exchange-dependent relaxation (AREX); MTR asymmetry; normalized MT exchange rate and pool size product; direct water saturation peak width; and the observed T_1 and T_2. Regions of interests (ROIs) were manually contoured on the post-Gd T_1w. The mean (of median ROI values) was compared between groups. Clinical outcomes were determined by clinical and radiologic follow-up or histopathology.
Statistical Tests: t-Test, univariable and multivariable logistic regression, receiver operating characteristic, and area under the curve (AUC) with sensitivity/specificity values with the optimal cut point using the Youden index, Akaike information criterion (AIC), Cohen's d. $P < 0.05$ with Bonferroni correction was considered significant.
Results: Seven metrics showed significant differences between RN and TP. The high-power MTR showed the highest AUC of 0.88, followed by low-power MTR (AUC = 0.87). The combination of low-power CEST scans improved the separation compared to individual parameters (with an AIC of 70.3 for low-power MTR/AREX). Cohen's d effect size showed that the MTR provided the largest effect sizes among all metrics.
Data Conclusion: Significant differences between RN and TP were observed based on saturation transfer MRI.
Evidence Level: 3
Technical Efficacy: Stage 2

*Address reprint requests to: H.M., 2075 Bayview Ave, Toronto, ON M4N 3M5, Canada.
E-mail: hatef.mehrabian@mail.utoronto.ca
Hatef Mehrabian and Rachel W. Chan contributed equally to this work as first authors.
Hany Soliman and Greg J. Stanisz contributed equally to this work as senior authors.

From the [1]Physical Sciences Platform, Sunnybrook Research Institute, Toronto, Ontario, Canada; [2]Department of Radiation Oncology, Sunnybrook Health Sciences Centre, University of Toronto, Toronto, Ontario, Canada; [3]Department of Medical Biophysics, University of Toronto, Toronto, Ontario, Canada; and [4]Department of Neurosurgery and Pediatric Neurosurgery, Medical University of Lublin, Lublin, Poland

Additional supporting information may be found in the online version of this article

Brain metastases (BM) are the most commonly diagnosed intracranial neoplasms. BM develop in nearly 30% of all cancer patients.[1,2] Over the past decade, stereotactic radiosurgery (SRS), which delivers a focal dose of radiation locally to the tumor, has become part of the treatment for many patients with BM. This is due to the frequently observed consequence of cognitive decline with whole brain radiotherapy and improved targeting in radiation treatment.[3] However, the high ablative doses used in SRS can lead to late radiation necrosis (RN) in up to 5%–25% of patients.[4] Differentiating these radiation-induced changes from tumor progression (TP) using conventional MRI is challenging, given that both RN and TP frequently appear as enhancing lesions on post-gadolinium (Gd) T_{1w}-weighted (T_{1w}) MRI, with increased vasogenic edema on T_2-weighted (T_{2w}) fluid-attenuated inversion recovery (FLAIR) MRI.[5] As such, longer clinical follow-up with serial imaging, invasive surgical resection, or biopsy (when technically feasible) may be required to differentiate between RN and TP.[6] Imaging biomarkers with the potential to reliably distinguish these two inherently different conditions, at the time of the presentation of an enlarging enhancing lesion, are needed. This is important in clinical practice as TP may be treated with further oncological therapy (surgery and/or re-irradiation), while RN is managed with observation, steroids, or vascular endothelial growth factor inhibitors.

A promising MRI method is chemical exchange saturation transfer (CEST) imaging, which can measure the concentration and exchange of hydrogen protons in various chemical groups and metabolites.[7,8] Amide proton transfer (APT) CEST is sensitive to exchangeable protons including those of amide groups in proteins and peptides,[8–10] while the magnetization transfer (MT) signal arises from protons that are associated with macromolecules[11,12] including myelin and cell membrane lipids, and is an indicator of white matter integrity. APT CEST and relayed nuclear Overhauser effect (rNOE) have shown promising results in differentiating radiation-induced side effects from viable tumor in both preclinical[9] and clinical studies.[13,14] Specifically, a pre-clinical study successfully differentiated viable tumor from pseudo-progression in a mouse model of glioma.[9] A pilot clinical study of 16 BM patients scanned with CEST after SRS showed statistically significant separation between TP and RN based on a semi-quantitative CEST-based metric (i.e., magnetization transfer ratio [MTR]).[13] However, this previous study has used only a low saturation B_1 amplitude of 0.52 μT, whereas the pre-clinical study employed a higher radiofrequency (RF) amplitude of 2.0 μT.[9,13] Higher saturation power increases the APT effect, which could better sensitize CEST to different sub-populations of proteins and peptides.

In the present clinical study, we aimed to apply CEST using both high (2.0 μT) and low (0.52 μT) RF saturation amplitudes and quantitative magnetization transfer (qMT) imaging with extraction of various CEST- and qMT-based metrics for distinguishing RN from TP. It is hypothesized that these metrics from saturation transfer imaging (including both high and low powers for CEST) would be able to differentiate between RN and TP groups in a clinical setting.

Materials and Methods

The study was approved by the institutional review board and written informed consent was obtained from all patients.

Study Design

The eligibility criteria of this prospective cohort study included adult patients with BM treated with SRS (single-fraction or hypo-fractionated regimens), who presented with enlarging enhancing lesions detected on post-Gd T_{1w} MRI as part of their routine clinical scans between April 2020 and January 2021. The interval between SRS treatment and time of diagnosis was more than 3 months (516 ± 442 days) and CEST/qMT scan was performed within 1-week from diagnosis. Exclusion criteria included patients with contraindications to MRI, eGFR <30, weight >136 kg, with pacemakers, cerebral aneurysm clips, shrapnel injury or implantable electronic devices not compatible with MRI, or patients with severe claustrophobia. Patients had no additional radiation treatment between their initial SRS and the time of the qMT/CEST scans. In addition, qMT/CEST scans were performed more than 3 months after SRS treatment (with a mean time interval of 516 ± 442 days before the patient was recruited for the qMT/CEST scan) to avoid early post-treatment effects including inflammation that may confound the imaging results. Lesions with a diameter less than 0.6 cm were excluded to avoid partial volume effects. In this study, 16 patients (out of 86 patients who were recruited) were excluded due to a lack of clinical follow-up (n = 5), excessive artifacts due to motion during a CEST scan or between CEST and post-Gd T_{1w} scans (n = 3), a lesion smaller than 0.6 cm in diameter causing partial volume effects (n = 3), the CEST imaging slice being misaligned with the enhancing lesion (n = 2), a lesion ROI left with no analyzable CEST voxel remaining due to artifacts near the skull (n = 1), early termination of the exam due to claustrophobia (n = 1), and data irrevocably lost prior to backup storage (n = 1). After exclusion, a total of 70 patients (with 75 lesions) were included in the analysis.

Lesion Outcome

Patients were managed according to the standard of care for diagnosis and treatment of RN and TP. Differentiation between RN and TP was determined by a radiation oncologist (HS) with 12 years of experience who also took into account any results from histopathology, clinical reports by the managing radiation oncologists of the patients (AS, HS, SM, CT, ZH, JD) and radiology reports based on serial clinical follow-up imaging (with pre/post-Gadolinium T_1-weighted and FLAIR imaging, and if requested by the physician, dynamic susceptibility contrast perfusion imaging) over a clinical follow-up period with a minimum of 6 months (with an approximate range of 6–10 months) from the time of initial CEST imaging. The lesion was excluded from analysis if a definite outcome of TP or

RN could not be rendered due to insufficient follow-up (eg, due to patient not showing up to follow-up imaging or death) and due to other reasons for exclusion listed in the previous section above. If histopathology results were available (n = 11), the lesion was considered TP (or RN) if the histological assessment consisted of mostly tumor (or mostly necrosis) was observed, using a threshold of 80% as in a previous study.[13] If histopathology was not available, then the clinical outcomes from serial imaging follow-up examinations were based on the Response Assessment in Neuro-Oncology Brain Metastases criteria.[15]

MR Imaging

Images were acquired on a 3-T scanner (Achieva; Philips Medical Systems, Best, The Netherlands) with an eight-channel head coil. The MRI scans included: CEST using 970 msec RF saturation comprised of four block pulses (242.5 msec duration each, separated by 2.5 msec gaps) at high (2.0 µT) and low (0.52 µT) B_1 amplitudes, and reference scans at each end of the CEST spectrum for baseline drift correction; water saturation shift referencing (WASSR) scan[16] for main magnetic field inhomogeneity (B_0) correction; water shift and B_1 (WASABI) scan[17] for B_1 inhomogeneity correction; qMT

Table 1. Imaging parameters for each sequence in the MRI scan	
Scan	**Imaging Parameters**
CEST	Acquisition: TFE readout, FOV = 240 × 192 mm^2, slice thickness = 3 mm, acquisition matrix = 160 × 124, TR = 7.7 msec, TE = 4.5 msec, flip angle = 90°, SPIR fat suppression, TFE factor = 2, partial Fourier factor = 0.8, bandwidth = 287 Hz/pixel, resulting in 1.5 × 1.5 × 3 mm^3 resolution. Four block pulses (242.5 msec duration each, separated by 2.5 msec gaps) with nominal RF saturation B_1 = 0.52 µT (repeated twice) and 2.0 µT.
	CEST Z-spectrum: frequency offsets between −5.9 and 5.9 ppm in 0.2 ppm increments with three reference scans at −780 ppm before the spectrum and two afterwards. (Acquisition time: 4 minutes 35 sec per spectrum; for all three CEST scans: 13 minutes 45 sec).
WASSR	Acquisition and saturation pulse duration and blocks the same as CEST.
	RF saturation B_1 of 0.1 µT and frequency offsets between −1.2 and 1.2 ppm in 0.12 ppm increments (acquisition time: 1 minute 39 sec).
WASABI	Acquisition the same as CEST.
	RF saturation B_1 of 3.6 µT and saturation duration of 5 msec and frequency offsets between −2 and 2 ppm in 0.08 ppm increments. (Acquisition time: 1 minute 3 sec).
qMT	Acquisition and saturation pulse duration and blocks the same as CEST.
	Three MT spectra using RF saturation B_1 amplitudes of 1.5, 3, and 5 µT each at 14 frequency offsets logarithmically spaced between 3 and 780 ppm. (Acquisition time for all three qMT scans: 3 minutes 6 sec).
T_1 mapping	T_1 mapping was performed using an inversion recovery-prepared TSE with TI = 50, 160, 500, 1600, and 4500 msec. (Acquisition time: 1 minute)
T_2 mapping	Multiple echo GraSE sequence with TEs spanning 12 to 120 msec in 10 msec increments. (Acquisition time: 1 minute 40 sec).
Pre-Gd T_2-weighted FLAIR	FOV = 250 × 250 mm^2, slice thickness = 2 mm, matrix = 228 × 228 × 90, interpolated matrix = 320 × 320 × 90, TR = 4800 msec, TE = 262 msec, flip angle = 40°, SPIR fat suppression, TI = 1650 msec, TFE factor = 182, bandwidth = 1421 Hz/pixel. (Acquisition time: 7 minutes 7 sec).
Post-Gd T_{1w}	3D axial inversion-prepared TFE with FOV = 240 × 240 mm^2, slice thickness = 1 mm, matrix = 240 × 240 × 200, TR = 6.8 msec, TE = 3.1 msec, flip angle = 8°, TI = 900 msec, TFE factor = 120, bandwidth = 255 Hz/pixel. (Acquisition time: 5.7 minutes).

CEST = chemical exchange saturation transfer; TFE = turbo field echo; FOV = field of view; TR = repetition time; TE = echo time; SPIR = spectral presaturation with inversion recovery; RF = radiofrequency; WASSR = water saturation shift referencing; WASABI = simultaneous mapping of water shift and B1; qMT = quantitative magnetization transfer; TSE = turbo spin echo; TI = inversion time; GRaSE = gradient and spin echo; Gd = gadolinium contrast agent injection; T_{1w} = T_1-weighted.

scan comprised of three MT spectra with $B_1 = 1.5$, 3, and 5 µT amplitudes; T_1 and T_2 mapping.

Since block pulses were used, the average B_1 values corresponded to the nominal B_1 amplitudes for CEST and qMT. These sequences were acquired on an axial slice passing through a representative slice of the lesion (with the largest cross section of the lesion manually chosen by the radiation oncologist) based on the enhancing regions on post-Gadolinium T_1-weighted imaging from the previous diagnostic scan. Three-dimensional (3D) T_{2W} FLAIR and 3D post-Gd T_{1w} scans were also acquired (total scanning time of approximately 45 minutes). Imaging parameters for all scans are reported in Table 1.

MR Analysis

The CEST, qMT, WASSR, WASABI, T_1, and T_2 images were co-registered to the first CEST reference image using affine registration in Elastix (v4.7, https://elastix.lumc.nl/).[18] After B_0 correction (determined from WASSR), three neighboring frequency offsets (i.e., 3.3, 3.5, and 3.7 ppm) were averaged to compute the MTR_{Amide} metric and to reduce noise in the Z-spectrum corresponding to the amide CEST peak. Similarly, for computing the MTR_{rNOE} metric, the spectrum amplitudes corresponding to frequency offsets of -3.7, -3.5, and -3.3 ppm were averaged. To correct for B_1 inhomogeneity (due to spatially varying RF power transmitted to each voxel), voxel-wise B_1 scaling factors were calculated (using WASABI) and the MTR maps were divided by these scaling factors. MTR asymmetry was also calculated using the following formula:

$$MTR_{asym} (3.5 \, ppm) = MTR_{Amide} - MTR_{rNOE},$$

where $MTR_{asym,2.0µT}$ (3.5 ppm) is equivalent to APT. The apparent exchange-dependent relaxation (AREX) metric aims at measuring the pure CEST effect by removing the MT effect and direct water saturation effect (DE) from the CEST spectrum.[19] To calculate AREX, the voxel-wise qMT parameters were estimated using the Bloch–McConnell equations in the transient state.[20,21] These parameters were then used to simulate an MT Z-spectrum (i.e., without CEST and rNOE contributions) with the saturation pulse parameters of the CEST experiment.[22] AREX was then computed using the simulated MT Z-spectrum (as Z_{ref}) and the measured CEST spectrum (as Z_{lab}) using the following formula[19,23]:

$$AREX = \left(\frac{1}{Z_{lab}} - \frac{1}{Z_{ref}}\right)/T_1,$$

which was followed by B_1 scaling (i.e., dividing the AREX map by the B_1 scaling factor). Similar to the MTR calculation, AREX values for three neighboring frequency offsets were averaged to calculate $AREX_{Amide}$ and $AREX_{rNOE}$. For qMT metrics, the MT exchange rate (RM_{0B}/R_A) and direct water saturation effect ($1/[R_A T_{2A}]$) were used.

The post-Gd T_{1w} and T_{2w} FLAIR images were re-sampled at the CEST resolution and the slice corresponding to the CEST slice was co-registered to the CEST reference image. Enhancing tumor regions of interest (ROIs) were manually drawn (HM, confirmed by radiation oncologist HS with 12 years of experience) on the post-Gd T_{1w} images (on a single slice that corresponded to the scanned CEST/MT slice for each patient) and overlaid onto the CEST images for quantification. The ROIs were defined enclosing the whole contrast-enhancing lesions; for example, if a lesion consisted of an enhancing rim surrounding a hypointense core, the entire lesion was contoured and included for analysis. There were no additional margins added beyond the enhancing regions. For patients

Table 2. Patient and lesion characteristics

Number of lesions	75
Number of patients	70
Patients with two lesions	5
Gender	
Male	19 (21 lesions)
Female	51 (54 lesions)
Median age [range] (years)	60 [55–65]
Outcome	
Radiation necrosis	45
Tumor progression	30
Primary pathology	
NSCLC	34
SCLC	2
Breast	25
Melanoma	5
RCC	5
Thyroid	1
Esophagus	1
AVM	1
Nasopharynx	1
Treatment (dose/fraction)	
16.0–20.0 Gy/1 Fr	28
24.0–27.0 Gy/3 Fr	9
25.0–32.5 Gy/5 Fr	35
Other	3
Outcome determination method	
Histopathology	11
Imaging follow-up	64

NSCLC = Non-small cell lung cancer; SCLC = small cell lung cancer; RCC = renal cell carcinoma; AVM = arteriovenous malformation.
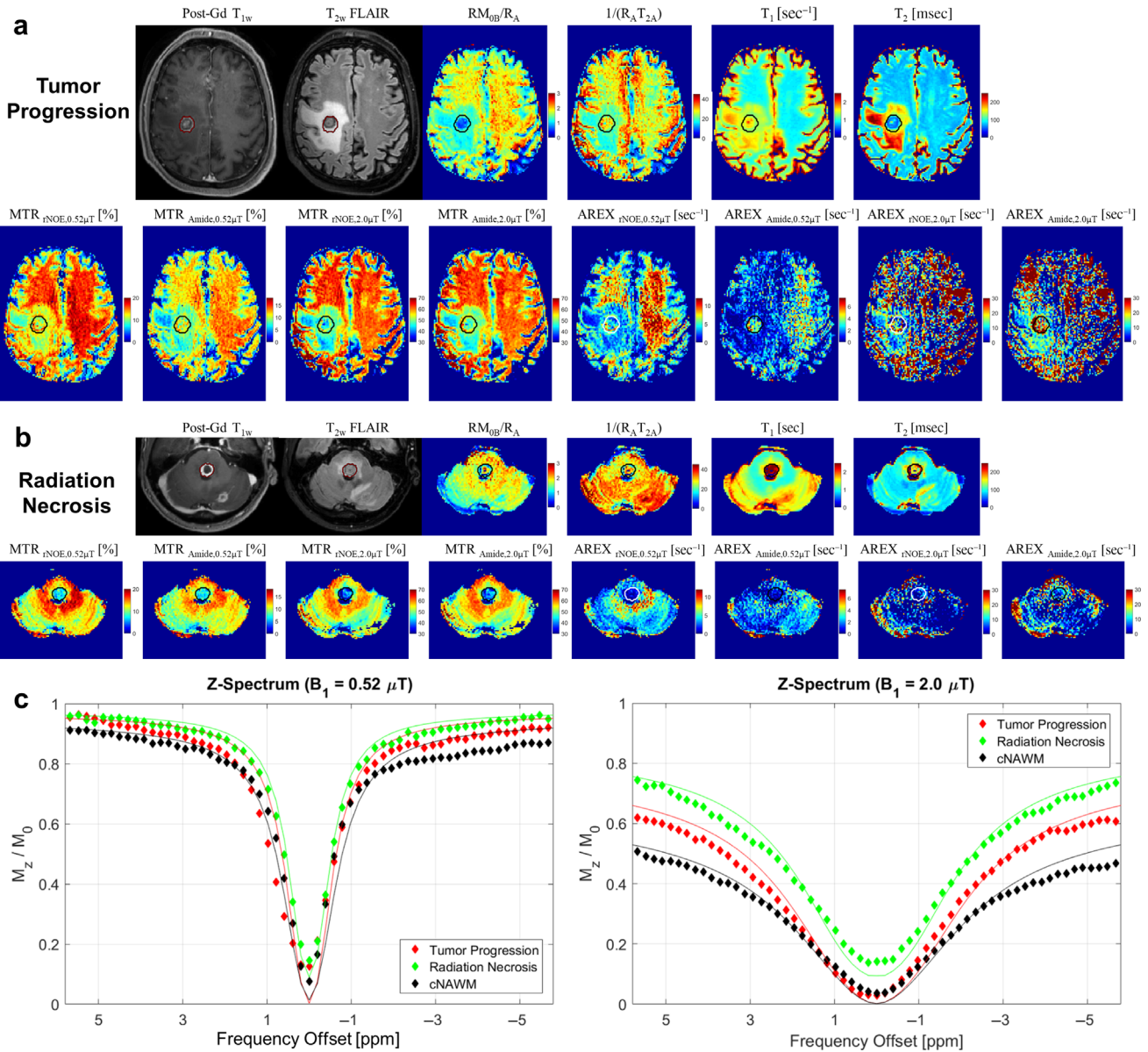
Figure 1: Structural MRI (post-Gd T_{1w} and T_{2w} fluid-attenuated inversion recovery) with chemical exchange saturation transfer, magnetization transfer (MT), T_1, and T_2 parametric maps for (a) a representative lesion diagnosed clinically as tumor progression and (b) a representative lesion diagnosed clinically as radiation necrosis. The regions of interests represent manually drawn contours, over the whole lesion, based on post-gadolinium T_1-weighted imaging. (c) Z-spectra for the representative lesions (from a and b) along with a normal appearing white matter region are shown for $B_1 = 0.52$ and 2.0 μT. The dots represent measurements and the lines represent the extrapolated MT spectra.

who had previous surgery, the surgical cavity was excluded from the ROI. All metrics were computed voxel-wise and the median metric values over the lesion ROIs were calculated.

Statistical Analysis

Analyses were performed using MATLAB (R2016b; The MathWorks, Natick, MA) and R software (v4.0.2; The R Foundation for Statistical Computing, Vienna; https://www.r-project.org/). Differences in each of the 14 parameter values (i.e., those of MTR, AREX, qMT and the observed T_1 and T_2) between RN and TP ROIs were compared using two-sample t-tests. Cohen's d, which quantifies the magnitude of differences between the two population averages relative to the spread,[24] was also computed to quantify the effect size for all parameters (i.e., those of MTR, AREX, qMT and the observed T_1 and T_2).

The ability of individual parameters to predict RN versus TP was investigated using univariable logistic regression. Model performance for univariable models was assessed in terms of the ability of the models to discriminate RN from TP using the receiver operating characteristic (ROC) curve with the area under the curve (AUC). For multivariable models, multivariable logistic regression was performed by considering each metric as an independent variable in the model. The Akaike information criterion (AIC) was also determined. The AIC is a measure of how well a logistic regression model fits the current data, where a penalizing term is added for models that contain a large number of predictors (independent variables) to reduce

overfitting. The AIC was also calculated for univariable logistic regression models and was used to compare the different uni- and multivariable models (i.e., the lower the AIC, the better the model performance). The Youden index was used to determine the optimal cut-off point on the ROC curve for each metric, and the sensitivity and specificity values associated with this optimal cut-off point were determined. Bonferroni correction for multiple testing was used for t-tests, where a two-sided P-value of ≤0.00357 (=0.05/14) was considered statistically significant.

Results

Data from 75 lesions (70 patients) were included in the final analysis, with 45 lesions classified as RN and 30 as TP. The SRS treatment included single-fraction SRS (16–20 Gy) and hypo-fractionated SRS (24–32.5 Gy in 3–5 fractions). The majority of lesions had breast cancer (n = 25) or non-small-cell lung cancer (n = 34) as the primary tumor and outcomes were determined through histopathology for 11 lesions and by imaging follow-up for 64 lesions. Table 2 reports further patient and lesion characteristics including the primary tumor type and radiation dose.

All CEST, MT, and DE metrics were calculated voxel-wise. Figure 1a,b shows the parametric maps for two representative patients with TP and RN, along with Z-spectra in Fig. 1c. Table 3 reports the mean and standard deviation (of the median parameter value in each ROI) over all lesions in each subcohort (TP or RN). All rNOE and amide MTR and AREX metrics at both RF powers as well as MT and DE were lower in RN compared to TP. T_1 and T_2 were higher in RN. The four MTR parameters (for high/low saturation and for amide/rNOE), the two low-power AREX parameters (for amide/rNOE), and the observed T_2 relaxation time provided a statistically significant differentiation of RN and TP after adjustment for multiple comparisons.

In order to quantify the magnitude of the separation, Cohen's d effect size, reported in Table 3, showed that the MTR provided the largest effect sizes among all metrics. Table 3 also shows the AUC and AIC derived from univariable logistic regression models. The sensitivity and specificity values are shown in Table 4 for the optimal cut-off point for each metric, determined using the Youden index. Figure 2 shows the ROC curves for differentiating RN from

Table 3. Mean ± standard deviation for T_1 T_2, CEST, and qMT parameters in each cohort, along with P-value, Cohen's d effect size, area under the ROC curve (AUC) and Akaike information criterion (AIC) for differentiation between the two cohorts

	Tumor Progression	Radiation Necrosis	P-value	Effect Size (Cohen's d)	AUC	AIC
$MTR_{rNOE,0.52\mu T}$ [%]	**10.2 ± 1.4**	**8.3 ± 1.6**	**<0.0001**	**1.26**	**0.82**	**78.4**
$MTR_{Amide,0.52\mu T}$ [%]	**9.0 ± 0.9**	**7.3 ± 1.4**	**<0.0001**	**1.43**	**0.87**	**72.8**
$AREX_{rNOE,0.52\mu T}$ [sec^{-1}]	**2.8 ± 1.2**	**2.0 ± 0.7**	**<0.001**	**0.84**	**0.72**	**91.7**
$AREX_{Amide,0.52\mu T}$ [sec^{-1}]	**2.1 ± 0.6**	**1.5 ± 0.9**	**0.002**	**0.74**	**0.81**	**94.7**
$MTR_{asym,0.52\mu T}$ (3.5 ppm) [%]	−1.2 ± 1.3	−1.0 ± 1.2	0.70	0.29	0.52	105
$MTR_{rNOE,2\mu T}$ [%]	**46.5 ± 2.7**	**41.2 ± 5.0**	**<0.0001**	**1.25**	**0.83**	**77.9**
$MTR_{Amide,2\mu T}$ [%]	**48.2 ± 2.2**	**42.2 ± 5.1**	**<0.0001**	**1.44**	**0.88**	**67.3**
$AREX_{rNOE,2\mu T}$ [sec^{-1}]	5.5 ± 2.5	4.6 ± 2.0	0.09	0.40	0.62	102.1
$AREX_{Amide,2\mu T}$ [sec^{-1}]	7.6 ± 3.2	5.8 ± 2.7	0.01	0.62	0.68	98.3
$MTR_{asym,2\mu T}$ (3.5 ppm) [%]	1.7 ± 1.5	1.2 ± 2.0	0.23	0.29	0.58	103
RM_{0B}/R_A	1.4 ± 0.2	1.2 ± 0.3	0.009	0.63	0.66	97.6
$1/(R_A T_{2A})$	29 ± 4	26 ± 6	0.005	0.69	0.73	96.6
T_1 [sec]	1.77 ± 0.19	1.94 ± 0.32	0.01	0.61	0.69	98.3
T_2 [msec]	**114 ± 26**	**140 ± 34**	**<0.001**	**0.85**	**0.74**	**92.0**

The AIC for a model with no predictors (maximum AIC) was 105.
AUC = area under the receiver operating characteristic curve; AIC = Akaike information criterion; MTR = magnetization transfer ratio; rNOE = relayed nuclear Overhauser effect; AREX = apparent exchange-dependent relaxation rate; MTR_{asym} = magnetization transfer ratio asymmetry; R = exchange rate between free water and MT pools; M_{0B} = equilibrium MT pool size; R_A = longitudinal relaxation rate of free water pool; T_{2A} = transverse relaxation time of free water pool.

Table 4. Sensitivity and specificity associated with optimal cut point determined by Youden index

	Cut Point	Specificity [%]	Sensitivity [%]
$MTR_{rNOE,0.52\mu T}$ [%]	**8.9**	**87**	**62**
$MTR_{Amide,0.52\mu T}$ [%]	**7.8**	**93**	**69**
$AREX_{rNOE,0.52\mu T}$ [sec^{-1}]	**1.95**	**83**	**60**
$AREX_{Amide,0.52\mu T}$ [sec^{-1}]	**1.6**	**80**	**82**
$MTR_{asym,0.52\mu T}$ [%]	−1.0	60	56
$MTR_{rNOE,2\mu T}$ [%]	**44.3**	**83**	**76**
$MTR_{Amide,2\mu T}$ [%]	**45.1**	**93**	**73**
$AREX_{rNOE,2\mu T}$ [%]	5.0	53	76
$AREX_{Amide,2\mu T}$ [%]	6.9	63	82
$MTR_{asym,2\mu T}$ [%]	1.4	67	58
RM_{0B}/R_A	1.1	87	47
$1/(R_A T_{2A})$	24	97	44
T_1 [sec]	1.93	83	58
T_2 [msec]	**116**	**67**	**78**

MTR = magnetization transfer ratio; rNOE = relayed nuclear Overhauser effect; AREX = apparent exchange-dependent relaxation rate; APT = amide proton transfer; R = exchange rate between free water and MT pools; M_{0B} = equilibrium MT pool size; R_A = longitudinal relaxation rate of free water pool; T_{2A} = transverse relaxation time of free water pool.

TP for each metric. In Fig. 3, the four MTR parameters, which provided the best separation, are shown for each cohort. Plots for all the other metrics are shown in Fig. S1. Results from multivariable logistic regression, performed for different subsets of CEST, MT, and DE metrics, are shown in Table 5, where the AIC was calculated to assess the ability of the metric to predict TP without overfitting the data. At high power, combining multiple metrics (with AIC = 72.5) did not improve the discriminatory power when compared to using $MTR_{Amide,2.0\mu T}$ alone (with AIC = 67.3). However, combining the low power metrics improved the predictive power (eg, with AIC = 70.3 for low-power MTRs and AREXs) compared to individual MTRs (eg, AIC = 72.8 for $MTR_{Amide,0.52\mu T}$ alone).

Discussion

This study examined CEST as an imaging biomarker for differentiating RN from TP in a clinical setting among patients with BM. Significant differences were found in metabolic characteristics (AREX), macromolecular content (MT), and direct water saturation effect (DE) parameters between RN and TP. Among the 14 studied parameters, MTR_{Amide} resulted in the best separation with large effect sizes and the highest AUC for high and low RF powers, respectively. MTR represents a combination of the CEST, MT, and DE; all four MTR parameters showed significant differences between the two cohorts. Considering that the AUC and Cohen's d effect sizes for AREX, MT, and DE were similar, it appears that these components all contributed to the separation provided by MTR. Furthermore, $MTR_{Amide,2.0\mu T}$ provided the best separation.

Although statistical differences were significant among all plots of the MTR, the values for TP have lower variability compared to the corresponding necrosis group. We speculate that the tissues classified as RN were compositionally different. The contents of these ROIs can be any combination of irradiated necrotic tumor cells, hemorrhage, and perhaps residual tumor cells. In contrast, TP ROIs were likely to contain mainly active tumor cells. In RN, the hypointense APTw CEST signal from necrotic cores has been linked to morphological changes that include parenchymal coagulative necrosis, loss of normal brain tissue components, the presence of necrotic cells and damaged vessels.[9] In contrast, APTw CEST shows a hyperintense signal in viable, active tumor regions, seen on histology in a previous study using APTw CEST to differentiate between tumor and necrosis.[9] This has been attributed mainly to higher cytosolic content of proteins and peptides in tumors compared to normal cells,[9,25] which has been confirmed by measurements of increased protein
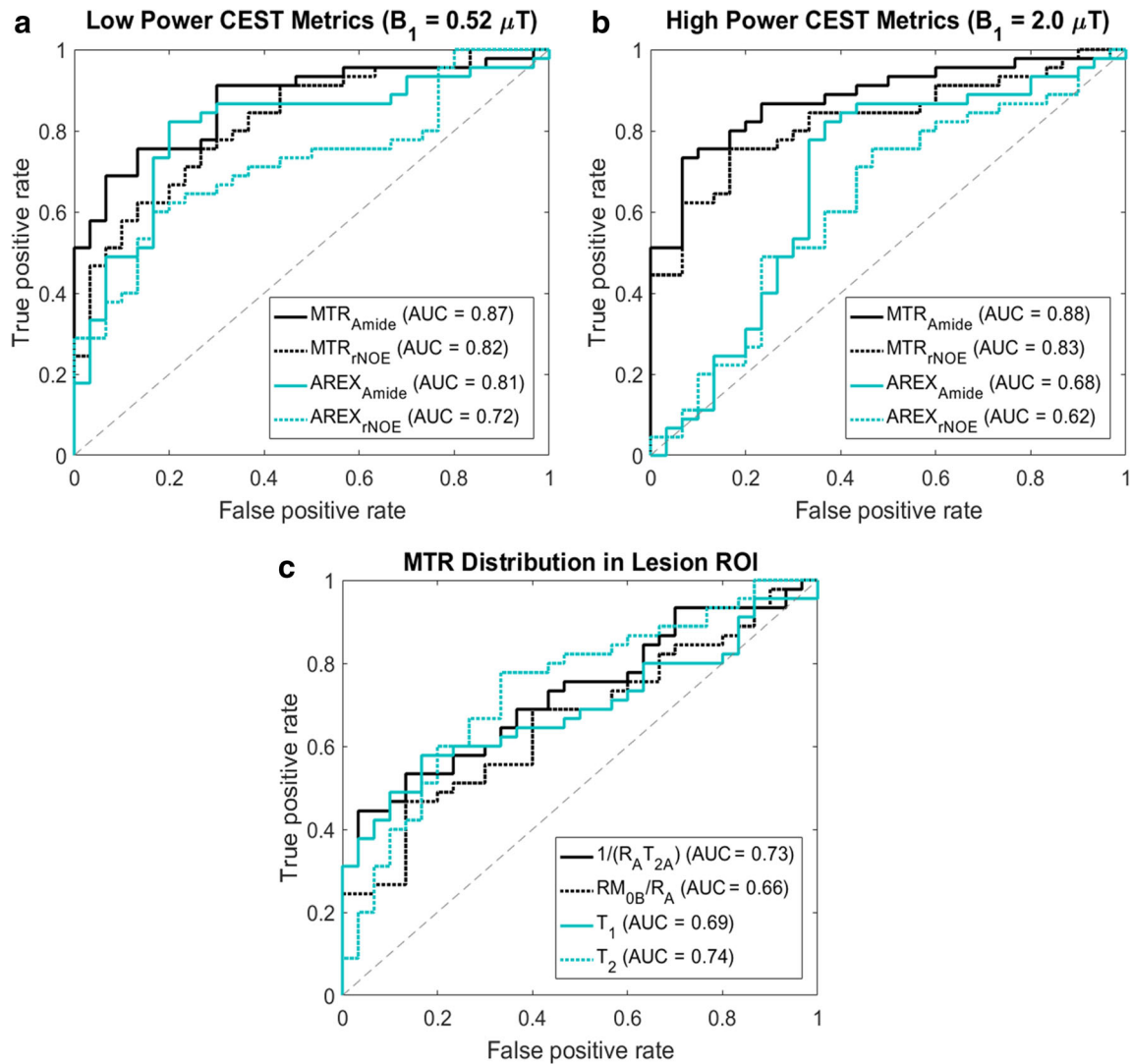
Figure 2: Receiver operating characteristic curves demonstrating the performance of each metric for the differentiation of radiation necrosis from tumor progression for (a) low power chemical exchange saturation transfer (CEST) metrics, (b) high power CEST metrics, and (c) magnetization transfer and direct effect metrics.

expression levels in tumor.[26] Among the other contributing factors, increased APT signal in tumors is also related to the slightly increased amide proton exchange rates.[25] MT was decreased in RN compared to that of tumor, which could be related to decreased semi-solid content in necrotic regions (due to decreased cellularity or lost integrity of cellular membranes). As all these effects contribute to the MTR, using quantitative CEST analysis to tease out different components may help for optimizing imaging protocols in the future.

Conventional CEST contrast is typically MTR asymmetry at ± 3.5 ppm. However, the subtraction of downfield CEST amide from upfield aliphatic rNOE signal can potentially diminish the contrast in the resultant image in the case where the signal from each offset varies in the same direction. As such, in our study, the signal from those offsets (i.e., amide at 3.5 ppm and rNOE at -3.5 ppm) were analyzed separately. The reason for using qMT, aside from

quantifying the semi-solid fraction and other macromolecule-related parameters, was to remove the contribution of MT from the MTR, which is sensitive to CEST, relayed nuclear Overhauser, MT and T_1 effects. The isolation of CEST effects was achieved through the AREX metric, which required the MT Z-spectra to be extrapolated and then removed from the measured Z-spectra at the same CEST offsets and B_1 amplitudes. The AREX metric had the added benefit of giving a resultant image that is free from any contributions from changes in T_1. However, AREX had low SNR since it relied on several experiments including MT, CEST and inversion recovery-prepared turbo spin echo (for T_1 mapping) and calculated the inverse of these measurements, which resulted in the noise being propagated and magnified.

The current study reported a larger overlap between the metrics compared to a previous pilot study (where several
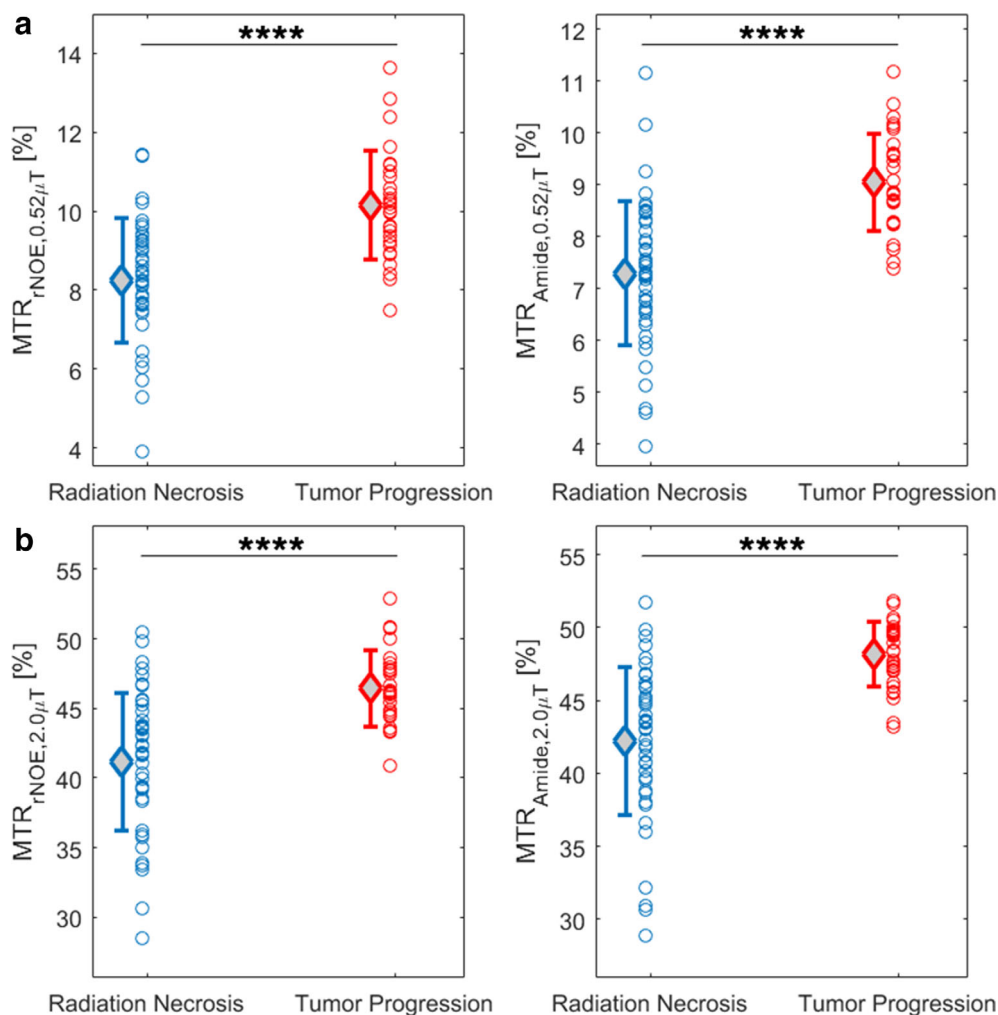
Figure 3: Plots of the (a) low-power and (b) high-power magnetization transfer ratio values are shown. Data points represent the median regions of interest values for each lesion. As well, the mean and standard deviation in each of the radiation necrosis and tumor progression cohorts are included. Statistically significant differences between the two cohorts are shown by asterisks (****$P < 0.0001$).

parameters provided perfect separation of the two conditions).[13] Specifically, this might be due to different patient characteristics, ROIs (spatial variation of the signal), or protocol differences. There were also differences in MRI characteristics between the two studies: the current study used a higher resolution (in-plane voxel = 1.5×1.5 mm^2 vs. 2.5×2.5 mm^2), and used a two-shot centrically encoded turbo field echo instead of single-shot echo-planar imaging readout. Moreover, in addition to the smaller sample size of the pilot study (n = 16), a major difference was the differing patient populations.[13] Patients in the pilot study were more likely to have undergone surgical resection (9 out of 16) after the CEST imaging and many were under surveillance for some time before recruitment.[13] The current patient population and recruitment-to-scan time might better represent the actual clinical practice as patients were recruited shortly after detection of the enlarging enhancing lesion during routine clinical follow-up and few (n = 11) underwent surgery or biopsy.

In the present study, multivariable logistic regression was explored, which allowed for comparisons across models with different numbers of predictors. Results from multivariable analysis showed that, while the combination of factors improved discrimination between TP and RN in certain parameter settings (i.e., for the low-power variables), it did not always result in higher predictive power (i.e., for the high-power B_1 setting). Reasons could be related to inherent CEST signal differences between high and low power and their differing dependence on the individual contributions of MT, CEST, or DE. Another reason could be related to the MTR, qMT, and AREX variables being correlated and, thus, may have similar information. The B_1 value for the low power was based on a previous study.[13] The higher B_1 amplitude of 2.0 μT was determined heuristically based on tumor conspicuity; this also matched the suggested B_1 amplitude in the consensus recommendations for APTw imaging of brain tumors.[25] However, another study has shown that APT imaging at 3.5 ppm using $B_{1,RMS} = 1.0$ μT performed on two

Table 5. Akaike information criterion for differentiation between the two cohorts for different combinations of CEST, MT, and direct effect metrics from multivariable logistic regression

Parameter Set	AIC
ALL	
High & low power MTR (Amide & rNOE)	72.8
High & low power AREX (Amide & rNOE)	
MT & direct effect	
T_1 & T_2	
ALL CEST and T_1 & T_2	
High & low power MTR (Amide & rNOE)	69.2
High & low power AREX (Amide & rNOE)	
T_1 & T_2	
ALL CEST & MT	
High & low power MTR (Amide & rNOE)	73.9
High & low power AREX (Amide & rNOE)	
MT & direct effect	
ALL CEST	
High & low power MTR (Amide & rNOE)	70.2
High & low power AREX (Amide & rNOE)	
High power CEST	
High power MTR (Amide & rNOE)	72.5
High power AREX (Amide & rNOE)	
Low power CEST	
Low power MTR (Amide & rNOE)	70.3
Low power AREX (Amide & rNOE)	
ALL MTR	
High & low power MTR (Amide & rNOE)	69.6
ALL AREX	
High & low power AREX (Amide & rNOE)	94.0
ALL Amide	
High & low power MTR (Amide)	71.0
High & low power AREX (Amide)	
MTR Amide	
High & low power MTR (Amide)	68.3
AREX Amide	
High & low power MTR (Amide)	95.8
ALL rNOE	

Table 5. Continued

Parameter Set	AIC
High & low power MTR (rNOE)	80.1
High & low power AREX (rNOE)	
MTR rNOE	
High & low power MTR (rNOE)	76.1
AREX rNOE	
High & low power AREX (rNOE)	93.6
MT & direct effect	96.0

AIC = Akaike information criterion; MTR = magnetization transfer ratio; rNOE = relayed nuclear Overhauser effect; AREX = apparent exchange-dependent relaxation rate; MT = magnetization transfer; CEST = chemical exchange saturation transfer.

human brains also results in an appropriate APT effect[27] suggesting that the inclusion of saturation with low power (in addition to high power) is still beneficial. Also, the steady-state optimal B_1 amplitude has been described for a system with a free water pool and a CEST pool.[28] It is a function of the T_1 and T_2 of the free water pool, the solute-to-free-water-pool exchange rate k_s, and frequency offset. It provides the optimal B_1 for amide CEST and aliphatic rNOE contrast 2.0 and 0.66 μT, respectively. This is another reason to measure over a range of B_1 amplitudes.

In future studies, including perfusion imaging or other MRI contrasts to provide more independent characteristics of the lesions may improve the predictive power when combined with MT and CEST imaging.

Specifically, future studies investigating differentiation between RN and TP could benefit from the combination of MT and CEST with dynamic susceptibility contrast (DSC)-MRI, where high perfusion suggests TP and low perfusion indicates RN.[5,29–32] MR spectroscopy (MRS) has also been proposed and high levels of choline, choline-to-creatine ratios, or choline-to-N-acetylaspartate (NAA) ratios are associated with progressive tumor burden.[30,33,34] A recent study showed that tumor habitat analysis on structural MRI has the potential to detect and localize viable tumor parts after SRS.[35] Other MRI contrasts that have shown encouraging results in differentiating RN from TP include diffusion-weighted imaging (DWI),[36] intra-voxel incoherent motion-DWI,[37] and dynamic contrast enhanced-MRI.[31,38] Additionally, future multi-vendor or multi-center studies would be required to further evaluate CEST, where parameters could be optimized based on a recently published consensus for APT CEST, which aimed at increasing the reproducibility and clinical applicability across centers.[25]
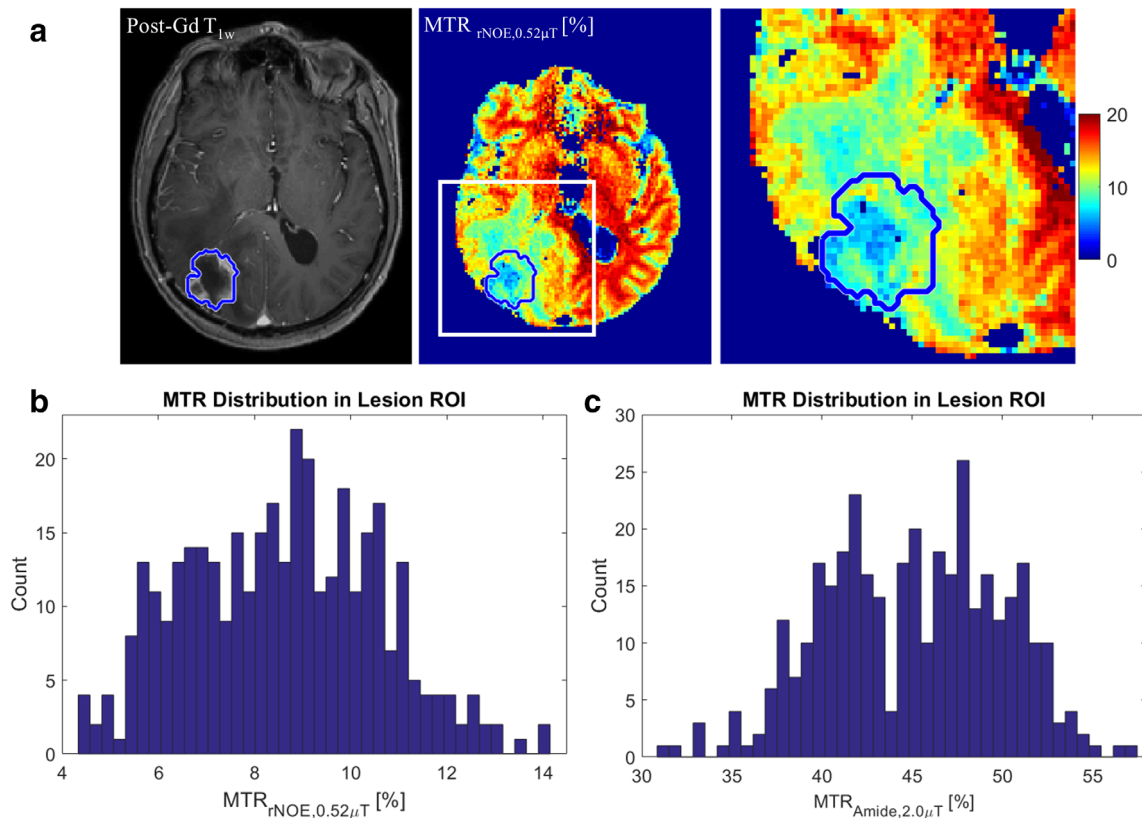
Figure 4: (a) $MTR_{rNOE,0.52\mu T}$ map for low power chemical exchange saturation transfer (CEST) for a patient along with (b) the histogram of this metric value in the lesion. The lesion includes a large number of voxels with high magnetization transfer ratio (MTR) values (in the tumor range) as well as a large number of voxels with low chemical exchange saturation transfer (CEST) values (in the radiation necrosis range). The clinical outcome of this lesion is progressive tumor. However, the presence of a large number of voxels with low MTR values lead to the incorrect diagnosis of radiation necrosis when using $MTR_{rNOE,0.52\mu T}$. (c) Using MTR of Amide at high power ($MTR_{Amide,2.0\mu T}$) on the other hand, suggests that the lesion is tumor, which highlights the need for considering multiple metrics. There are also two distinct metric value clusters in $MTR_{Amide,2.0\mu T}$ histogram suggesting presence of large areas of both tumor and radiation necrosis. A detailed analysis of the histogram also suggests the presence of a large region with viable tumor even at the low power CEST.

Limitations

This study demonstrated the limitation of the technique for small lesions (less than 0.6 cm in diameter) due to partial volume effects. Normal white matter has higher MTR (and higher MT) compared to both TP and RN; thus, any inclusion of white matter in the analysis ROI would be problematic. This issue becomes relevant when there are very few voxels in the lesion ROI and if the majority of them partially contain white matter. Moreover, since the lesion was delineated on the post-Gd T_{1w} scans, for small lesions any head motion would result in the ROI being incorrectly placed in a white matter region.

A major limitation of the current study was the difficulty in selecting the CEST slice through a representative cross section of the lesion. The largest cross section was used, but there could have been error and it was difficult to select this when the lesion was small. A 3D CEST acquisition would solve this issue and could be able to capture any heterogeneity including any mixture of tumor and necrosis across slices. The ROIs were manually drawn on contrast-enhancing regions of post-Gd T_{1w} MRI. The enhancement pattern can be heterogeneous and using automatic segmentation as well as probing sub-regions could improve performance particularly with 3D CEST. Another limitation of our study was that the information on the radiation dose and fraction scheme was not taken into account. As RN is known to depend on both, these variables could be used to help determine TP or RN, potentially with higher accuracy. Furthermore, this study aimed at binary classification of the lesions. However, most lesions have both tumor and necrosis parts.[39,40] This poses a challenge for the determination of the best metrics. Since CEST allows relatively high spatial resolution, this is amenable to histogram analysis of voxels within the ROI (as illustrated in Fig. 4).

Conclusion

Significant differences between RN and TP were observed based on measures from CEST and MT imaging. Hence, saturation transfer MRI may facilitate differentiation of RN from TP.

Acknowledgment

REFERENCES

1. Scoccianti S, Ricardi U. Treatment of brain metastases: Review of phase III randomized controlled trials. Radiother Oncol 2012;102:168-179. https://doi.org/10.1016/j.radonc.2011.08.041.

2. Nayak L, Lee EQ, Wen PY. Epidemiology of brain metastases. Curr Oncol Rep 2012;14:48-54. https://doi.org/10.1016/B978-0-12-811161-1.00002-5.

3. Niranjan A, Monaco E, Flickinger J, Lunsford LD. Guidelines for multiple brain metastases radiosurgery. Prog Neurol Surg 2019;34:100-109. https://doi.org/10.1159/000493055.

4. Donovan EK, Parpia S, Greenspoon JN. Incidence of radionecrosis in single-fraction radiosurgery compared with fractionated radiotherapy in the treatment of brain metastasis. Curr Oncol 2019;26(3):e328-e333. https://doi.org/10.3747/co.26.4749.

5. Hoefnagels FWA, Lagerwaard FJ, Sanchez E, et al. Radiological progression of cerebral metastases after radiosurgery: Assessment of perfusion MRI for differentiating between necrosis and recurrence. J Neurol 2009;256:878-887. https://doi.org/10.1007/s00415-009-5034-5.

6. Ross DA, Sandler HM, Balter JM, Hayman JA, Archer PG, Auer DL. Imaging changes after stereotactic radiosurgery of primary and secondary malignant brain tumors. J Neurooncol 2002;56:175-181. https://doi.org/10.1023/a:1014571900854.

7. Ward K, Aletras A, Balaban R. A new class of contrast agents for MRI based on proton chemical exchange dependent saturation transfer (CEST). J Magn Reson 2000;143:79-87. https://doi.org/10.1006/jmre.1999.1956.

8. Zhou J, Payen J-F, Wilson DA, Traystman RJ, van Zijl PCM. Using the amide proton signals of intracellular proteins and peptides to detect pH effects in MRI. Nat Med 2003;9:1085-1090. https://doi.org/10.1038/nm907.

9. Desmond KL, Moosvi F, Stanisz GJ. Mapping of amide, amine, and aliphatic peaks in the CEST spectra of murine xenografts at 7 T. Magn Reson Med 2014;71:1841-1853. https://doi.org/10.1002/mrm.24822.

10. Zhou J, Tryggestad E, Wen Z, et al. Differentiation between glioma and radiation necrosis using molecular magnetic resonance imaging of endogenous proteins and peptides. Nat Med 2011;17:130-134. https://doi.org/10.1038/nm.2268.

11. Wolff SD, Balaban RS. Magnetization transfer contrast (MTC) and tissue water proton relaxationin vivo. Magn Reson Med 1989;10:135-144. https://doi.org/10.1002/mrm.1910100113.

12. Henkelman RM, Stanisz GJ, Graham SJ. Magnetization transfer in MRI: A review. NMR Biomed 2001;14:57-64. https://doi.org/10.1002/nbm.683.

13. Mehrabian H, Desmond KL, Soliman H, Sahgal A, Stanisz GJ. Differentiation between radiation necrosis and tumor progression using chemical exchange saturation transfer. Clin Cancer Res 2017;23:3667-3675. https://doi.org/10.1158/1078-0432.CCR-16-2265.

14. Desmond KL, Mehrabian H, Chavez S, et al. Chemical exchange saturation transfer for predicting response to stereotactic radiosurgery in human brain metastasis. Magn Reson Med 2017;78:1110-1120. https://doi.org/10.1002/mrm.26470.

15. Lin NU, Lee EQ, Aoyama H, et al. Response assessment criteria for brain metastases: Proposal from the RANO group. Lancet Oncol 2015;16:e270-e278. https://doi.org/10.1016/S1470-2045(15)70057-4.

16. Kim M, Gillen J, Landman BA, Zhou J, van Zijl PCM. Water saturation shift referencing (WASSR) for chemical exchange saturation transfer (CEST) experiments. Magn Reson Med 2009;61:1441-1450. https://doi.org/10.1002/mrm.21873.

17. Schuenke P, Windschuh J, Roeloffs V, Ladd ME, Bachert P, Zaiss M. Simultaneous mapping of water shift and B 1 (WASABI)—Application to field-inhomogeneity correction of CEST MRI data. Magn Reson Med 2017;77:571-580. https://doi.org/10.1002/mrm.26133.

18. Klein S, Staring M, Murphy K, Viergever MA, Pluim J. Elastix: A toolbox for intensity-based medical image registration. IEEE Trans Med Imaging 2010;29:196-205. https://doi.org/10.1109/TMI.2009.2035616.

19. Zaiss M, Windschuh J, Paech D, et al. Relaxation-compensated CEST-MRI of the human brain at 7T: Unbiased insight into NOE and amide signal changes in human glioblastoma. Neuroimage 2015;112:180-188. https://doi.org/10.1016/j.neuroimage.2015.02.040.

20. Mehrabian H, Myrehaug S, Soliman H, Sahgal A, Stanisz GJ. Quantitative magnetization transfer in monitoring glioblastoma (GBM) response to therapy. Sci Rep 2018;8:2475. https://doi.org/10.1038/s41598-018-20624-6.

21. Mehrabian H, Lam WW, Myrehaug S, Sahgal A, Stanisz GJ. Glioblastoma (GBM) effects on quantitative MRI of contralateral normal appearing white matter. J Neurooncol 2018;139:97-106. https://doi.org/10.1007/s11060-018-2846-0.

22. Heo H-Y, Zhang Y, Jiang S, Lee D-H, Zhou J. Quantitative assessment of amide proton transfer (APT) and nuclear overhauser enhancement (NOE) imaging with extrapolated semisolid magnetization transfer reference (EMR) signals: II. Comparison of three EMR models and application to human brain glioma at 3 tesla. Magn Reson Med 2016;75:1630-1639. https://doi.org/10.1002/mrm.25795.

23. Lam WW, Oakden W, Karami E, et al. An automated segmentation pipeline for intratumoural regions in animal xenografts using machine learning and saturation transfer MRI. Sci Rep 2020;10:8063. https://doi.org/10.1038/s41598-020-64912-6.

24. Cohen J. Statistical power analysis for the behavioral sciences. New York, NY: Routledge Academic; 1988.

25. Zhou J, Zaiss M, Knutsson L, et al. Review and consensus recommendations on clinical APT-weighted imaging approaches at 3T: Application to brain tumors. Magn Reson Med 2022;88:546-574. https://doi.org/10.1002/mrm.29241.

26. Hobbs SK, Shi G, Homer R, Harsh G, Atlas SW, Bednarski MD. Magnetic resonance image-guided proteomics of human glioblastoma multiforme. J Magn Reson Imaging 2003;18:530-536. https://doi.org/10.1002/jmri.10395.

27. Kanazawa Y, Fushimi Y, Sakashita N, Okada T, Arakawa Y, Miyazaki M. B1 power optimization for chemical exchange saturation transfer imaging: A phantom study using egg white for amide proton transfer imaging applications in the human brain. Magn Reson Med Sci 2018;17:86-94. https://doi.org/10.2463/mrms.tn.2016-0069.

28. Zaiss M, Jin T, Kim S, Gochberg DF. Theory of chemical exchange saturation transfer MRI in the context of different magnetic fields. NMR Biomed 2022;1-21. online ahead of print. https://doi.org/10.1002/nbm.4789.

29. Sugahara T, Korogi Y, Tomiguchi S, et al. Posttherapeutic intraaxial brain tumor: The value of perfusion-sensitive contrast-enhanced MR imaging for differentiating tumor recurrence from nonneoplastic contrast-enhancing tissue. Am J Neuroradiol 2000;21:901-909.

30. Huang J, Wang AM, Shetty A, et al. Differentiation between intra-axial metastatic tumor progression and radiation injury following fractionated radiation therapy or stereotactic radiosurgery using MR spectroscopy, perfusion MR imaging or volume progression modeling. Magn Reson Imaging 2011;29:993-1001. https://doi.org/10.1016/j.mri.2011.04.004.

31. Knitter JR, Erly WK, Stea BD, et al. Interval change in diffusion and perfusion MRI parameters for the assessment of pseudoprogression in cerebral metastases treated with stereotactic radiation. Am J Roentgenol 2018;211:168-175. https://doi.org/10.2214/AJR.17.18890.

32. Muto M, Frauenfelder G, Senese R, et al. Dynamic susceptibility contrast (DSC) perfusion MRI in differential diagnosis between radionecrosis and neoangiogenesis in cerebral metastases using rCBV, rCBF and K2. Radiol Med 2018;123:545-552. https://doi.org/10.1007/s11547-018-0866-7.

33. Chuang M-T, Liu Y-S, Tsai Y-S, Chen Y-C, Wang C-K. Differentiating radiation-induced necrosis from recurrent brain tumor using MR perfusion and spectroscopy: A meta-analysis. PLoS One 2016;11:e0141438. https://doi.org/10.1371/journal.pone.0141438.

34. Weybright P, Sundgren PC, Maly P, et al. Differentiation between brain tumor recurrence and radiation injury using MR spectroscopy. Am J Roentgenol 2005;185:1471-1476. https://doi.org/10.2214/AJR.04.0933.

35. Lee DH, Park JE, Kim N, et al. Tumor habitat analysis by magnetic resonance imaging distinguishes tumor progression from radiation necrosis in brain metastases after stereotactic radiosurgery. Eur Radiol 2022;32:497-507. https://doi.org/10.1007/s00330-021-08204-1.

36. Hein PA, Eskey CJ, Dunn JF, Hug EB. Diffusion-weighted imaging in the follow-up of treated high-grade gliomas: Tumor recurrence versus radiation injury. Am J Neuroradiol 2004;25:201-209.

37. Detsky JS, Keith J, Conklin J, et al. Differentiating radiation necrosis from tumor progression in brain metastases treated with stereotactic radiotherapy: Utility of intravoxel incoherent motion perfusion MRI and correlation with histopathology. J Neurooncol 2017;134:433-441. https://doi.org/10.1007/s11060-017-2545-2.

38. Umemura Y, Wang D, Peck KK, et al. DCE-MRI perfusion predicts pseudoprogression in metastatic melanoma treated with immunotherapy. J Neurooncol 2020;146:339-346. https://doi.org/10.1007/s11060-019-03379-6.

39. Prasanna P, Rogers L, Lam TC, et al. Disorder in pixel-level edge directions on T1WI is associated with the degree of radiation necrosis in primary and metastatic brain tumors: Preliminary findings. Am J Neuroradiol 2019;40:412-417. https://doi.org/10.3174/ajnr.A5958.

40. Qian DC, Weinberg BD, Neill SG, et al. Co-occurrence conundrum: Brain metastases from lung adenocarcinoma, radiation necrosis, and gliosarcoma. Case Rep Oncol 2021;14:487-492. https://doi.org/10.1159/000514297.